

# Hydroxyapatite growth on multiwall carbon nanotubes grown on titanium fibers from a titanium sheet

Loubna Chetibi · Amine Achour · Jerzy Peszke ·  
Djamel Hamana · Slimane Achour

Received: 26 May 2013 / Accepted: 13 September 2013 / Published online: 27 September 2013  
© Springer Science+Business Media New York 2013

**Abstract** Nano-hydroxyapatite (HA) was grown on functionalized multiwalled carbon nanotubes (MWCNTs) deposited on TiO<sub>2</sub> nanofibers (NFs) that were hydrothermally grown on Ti metal sheets. The HA was electrochemically grown on the MWCNTs/TiO<sub>2</sub> porous layer. It was found that the HA grows on the MWCNTs/TiO<sub>2</sub> NFs in the form of dense coating with nanorice grain-shaped. The incorporation of MWCNTs between HA and TiO<sub>2</sub> NFs has led to higher adhesion strength as measured by micro-scratching test indicating the benefit of MWCNTs on the improving the bonding strength of HA layer. The obtained coatings exhibit excellent corrosion resistance in simulated body fluid. It is expected that this simple route for

preparing the new HA/MWCNTs/TiO<sub>2</sub>/Ti-layered structure might be used not only in the biomedical field, but also in catalysis and biological sensing among others.

## Introduction

Titanium and titanium alloys are widely used to fabricate dental and orthopedic implants due to their high mechanical strength and toughness, excellent corrosion resistance in physiological environment, and good biocompatibility [1–3]. However, the bioinertness of the metallic surfaces inhibits the growth of bone tissue [4]. In order to overcome this shortage, hydroxyapatite (HA, Ca<sub>10</sub>(PO<sub>4</sub>)<sub>6</sub>(OH)<sub>2</sub>) has been applied as a coating on the metallic implants due to its similarity in chemical compositions, high biocompatibility, and osteoconductivity to bone tissue of human [5–8].

Carbon nanotubes (CNTs) are of particular interest in various applications as they exhibit high chemical and thermal stability, mechanical strength, flexibility, electrical and thermal conductivity as well as low density [9–11]. Recently, the unique biological and medical properties of CNTs have attracted considerable attention, and it is expected that biomaterials using CNTs are very promising as nanobiomaterials [12]. To optimize the use of CNTs, it is often necessary to assemble nanostructures onto their surface. The combination of CNTs and nanoparticles are expected to deliver exceptional performances in biomaterials [13, 14]. In general, the most of these nanocomposites used in biomaterials are TiO<sub>2</sub> nanoparticles linked to or coated on CNTs [15, 16]. Nowadays, sol–gel coating followed by a heat treatment at elevated temperatures is the most commonly adopted method to introduce inorganic phases onto the CNT substrate [17, 18]. For instance, the heat treatment required in sol–gel processes often causes phase

---

L. Chetibi · D. Hamana  
Unit of Materials Science and Applications, University of  
Constantine, 25000 Constantine, Algeria  
e-mail: Ch\_loubna@hotmail.com

D. Hamana  
e-mail: d\_hamana@yahoo.fr

A. Achour  
LAAS-CNRS, 7 Avenue du Colonel Roche, 31400 Toulouse,  
France  
e-mail: a\_aminph@yahoo.fr

J. Peszke  
Faculty of Solid State Physics, University of Silesia, Bankowa  
Str. 12, 40-007 Katowice, Poland  
e-mail: j.peszke@rocketmail.com

J. Peszke  
Dynamax Nanotechnology, Konduktorska Str. 39a,  
40-155 Katowice, Poland

S. Achour (✉)  
Ceramic Laboratory, University of Constantine,  
25000 Constantine, Algeria  
e-mail: achourslimane11@yahoo.fr

detachment between the TiO<sub>2</sub> surface and underneath CNTs, agglomeration among neighboring TiO<sub>2</sub>/CNT cables and nonuniform crystallite. In all cases, the essential problem to be solved is the way to obtain a corrosion-resistant bioactive implant with better mechanical and biological properties and with good adhesion between HA coating and its substrate, especially those to be positioned in contact with bone like active prosthesis or functional matrices, etc. [4].

Recent reports indicated that modified Ti surface with high surface area of 1D TiO<sub>2</sub> nanostructure films brought about by the small particle size is beneficial to show better mechanical interlocking between HA and Ti than conventional micro-roughened Ti surface. It was also shown that the addition of CNTs between Ti and HA layers increases the hardness, elastic modulus, and interlaminar shear strength of the HA/CNT/Ti layers [19]. In this context, dense layer of HA–CNTs coatings were successfully developed on Ti substrate coated with TiO<sub>2</sub> nanotubes [20], using sol–gel method. Other studies have reported that nanostructured HA coatings have high chemical homogeneity, reduced flaw size, microstructural uniformity [21]. Moreover, the nanoscale roughness and grains as well as the high volume fraction of grain boundaries in nanostructured HA coatings can increase osteoblasts adhesion, proliferation, and mineralization [19, 21]. The combination of multiwalled carbon nanotubes (MWCNTs) and HA might be applicable not only in biomedical fields, but also in catalysis, biological sensing, and others [22, 23]. As a matter of fact, it would be interesting to combine mechanical and biological properties of the individual materials (Ti, TiO<sub>2</sub>, CNTs, and HA) layer by layer to obtain a single material with higher mechanical and biological properties.

This work reports on the preparation and characterization of a system consisting of HA layer with a novel nanorice grain-shaped, grown on MWCNTs/TiO<sub>2</sub> nanofibers/bulk Ti-layered structure, using low temperature simple methods. To the best of our knowledge this is the first time that HA, in the form of nanorice, is deposited on a highly porous nanostructure consisting of TiO<sub>2</sub> nanofibers (NFs) that were grown on Ti and coated with functionalized MWCNTs.

## Experimental

### Materials

#### *Preparation of anatase TiO<sub>2</sub> NF films*

Pure titanium specimens with sizes 15 × 20 × 3 mm<sup>3</sup> were mechanically polished, then treated by sonicating in ethanol and pickling in a 5 wt% oxalic acid solution at 100 °C for 2 h, followed by rinsing with distilled water and drying. A cleaned and homogeneous coarse surface of Ti samples was

obtained. The obtained specimens were soaked in a mixed solution of 16 ml H<sub>2</sub>O<sub>2</sub> (30 wt%) and 16 ml NaOH (10 M) in a Teflon autoclave. The autoclave was maintained at 80 °C for 24 h. After the autoclave was cooled to room temperature, the Ti plate was gently rinsed with distilled water. Thereafter, the as-prepared Ti sample was protonated through two cycles of ion exchange in 50 ml 0.1 M HCl for 2 h, and subsequently taken out, rinsed to neutral with distilled water, dried at 80 °C for 1 h, and finally calcined at 400 °C for 1 h to obtain anatase NF films on the Ti surface.

#### *Functionalization and dispersion of MWCNTs*

The functionalization and dispersion experiments are carried out on functionalized MWCNTs. The detailed preparation process was as follows: (i) MWCNTs were prepared then functionalized by oxidation in a mixture solution of HNO<sub>3</sub>+HCl in order to obtain ammonium salt of carboxylated carbon nanotubes (MWCNTs–COONH<sub>4</sub>). (ii) A 0.2 mg of functionalized MWCNTs was dispersed in a mixture consisting 0.02 mg polyvinylpyrrolidone and 40 ml distilled water, under ultrasonic treatment during 4 h.

#### *Impregnation of TiO<sub>2</sub> with MWCNTs*

The Ti sheets coated with TiO<sub>2</sub> NF film were introduced in a sealed container and kept under vacuum (10<sup>−2</sup> mbar) for 15 min, then the solution containing the dispersed MWCNTs was injected on the Ti sheet surface by opening a valve which separates the sealed container from the solution. After that, the samples were gently rinsed with distilled water and dried at 80 °C. During this process many MWCNTs were entrapped in the TiO<sub>2</sub> NF network.

#### *HA deposition*

Electrodeposition of HA was conducted at room temperature in an electrolyte containing 0.04 mol/l CaCl<sub>2</sub>, 0.027 mol/l (NH<sub>4</sub>)<sub>2</sub>HPO<sub>4</sub>, and 3 % H<sub>2</sub>O<sub>2</sub>. Thus, this solution is in Ca to P molar ratio of 1.67 with a pH value adjusted to 6.5, which is near to body condition. The deposition was carried out by applying a constant potential of 3 V. The solution was stirred during electrodeposition to obtain a uniform electrolyte concentration. The obtained coating was further treated in 0.1 mol/l NaOH solution at 80 °C for 2 h. Then the coated titanium cathodes were rinsed with distilled water and dried at 80 °C for 1 h. The prepared layered structure (HA/MWCNTs/TiO<sub>2</sub> NFs/Ti) is sketched in Fig. 1.

#### Characterization methods

The surface morphology of TiO<sub>2</sub> NFs, MWCNTs/TiO<sub>2</sub> NFs, and HA/MWCNTs/TiO<sub>2</sub> NFs were observed by

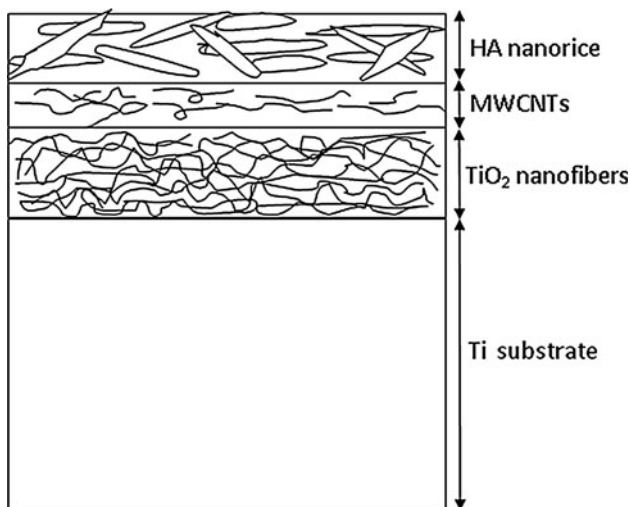


**Fig. 1** Schematic of the prepared layered structure

means of scanning electron microscopy (FE-SEM, Nova nano SEM 630) and transmission electron microscope (TEM, Titan). X-ray photoelectron spectra (XPS) studies were carried out in a Kratos Axis Ultra DLD spectrometer equipped with a monochromatic Al  $K\alpha$  X-ray source ( $h\nu = 1486.6$  eV) operating at 150 W, a multi-channel plate and delay line detector under vacuum of  $1.0 \times 10^{-12}$  bar. The survey and high-resolution spectra were collected at fixed analyzer pass energies of 160 and 20 eV, respectively. The instrument work function was calibrated to give an Au  $4f_{7/2}$  metallic gold binding energy (BE) of 83.95 eV and the spectrometer dispersion was adjusted to give a BE of 932.63 eV for metallic Cu  $2p_{3/2}$ . To avoid differential charging the samples were mounted in floating mode. The crystallinity and the structure of the HA coating was examined using X-ray diffractometry (Bruker D-8 Advance powder diffractometer). Data were collected using Cu  $K\alpha$  X rays at 40 kV and 30 mA. The coatings were also characterized by Raman spectroscopy and Fourier transform infrared FT-IR. The Raman spectra were recorded by a LAB RAM ARAMIS using cobalt laser source, and the Fourier transform infrared traces were obtained by using a Nicolet 6700 FT-IR system with continuum IR microscope in the wave number range of 600–4000  $\text{cm}^{-1}$ . The scratch tests were performed by using a Zwick testing machine of materials equipped with microindenter. Cyclic polarization data were carried out using an EG&G 273 potentiostat (263A), the obtained data are in the form of potential versus logarithmic current density curves. A conventional three-electrode set up was used for electrochemical measurement, with graphite as counter electrode and standard Ag/AgCl as reference electrode). The potential was increased at a rate of 5 mV/s, within a scan range of +3 V to  $-2$  V. The corrosion

parameters ( $I_{\text{corr}}$ ,  $E_{\text{corr}}$ , and  $R_p$ ) were calculated using 352SoftCorr III software.

#### Corrosion tests

Corrosion tests were carried out on uncoated and HA/MWCNTs coated  $\text{TiO}_2$  NFs films that are fixed in a cell exposing an area  $1 \text{ cm}^2$  in SBF solution at 37 °C. The SBF solution has the following ions concentrations: NaCl: 7.934 g/l;  $\text{NaHCO}_3$ : 0.350 g/l; KCl: 0.222 g/l;  $\text{K}_2\text{HPO}_4$ : 0.174 g/l;  $\text{MgCl}_2 \cdot 6\text{H}_2\text{O}$ : 0.303 g/l;  $\text{CaCl}_2$ : 0.545 g/l;  $\text{Na}_2\text{SO}_4 \cdot 10\text{H}_2\text{O}$ : 0.161 g/l [24, 25].

#### Results and discussion

Scanning electron microscope images for  $\text{TiO}_2$  NFs before and after incorporation of the functionalized MWCNTs are shown in Fig. 2. Figure 2a, b shows SEM micrographs of  $\text{TiO}_2$  NFs without incorporation of MWCNTs. It reveals that the treated Ti surface is well covered with an obvious network of  $\text{TiO}_2$  NFs like bundles having an average diameter of about 50 nm. Actually, these bundles are constituted of NFs with very small diameter (about 10 nm) as revealed by the TEM image of Fig. 3. The electron diffraction pattern presented in Fig. 3b was taken from fibers shown in Fig. 3a. It exhibits ring diameters equal to those corresponding to the crystalline anatase  $\text{TiO}_2$  phase. Figure 2c, d shows SEM images of the MWCNTs/ $\text{TiO}_2$  nanostructure, which show well dispersed many MWCNTs with an average diameter of about 20 nm and a length of several micrometers. It is clearly seen that the MWCNTs are homogeneously attached onto the surface of the  $\text{TiO}_2$  NFs. Also, it can be observed from these micrographs that the MWCNTs are bridged over the nanoporous structure, formed by the  $\text{TiO}_2$  NFs.

HRTEM of single  $\text{TiO}_2$  NF (Fig. 3c) shows well-crystallized anatase  $\text{TiO}_2$  NFs, but one can observe that the surface of the NFs is less crystallized than the inside due to the defects induced by chemical treatments used in its preparation. This irregular surface can increase the reaction between  $\text{TiO}_2$  NFs and MWCNTs.

The Raman spectra of  $\text{TiO}_2$  NFs and MWCNTs/ $\text{TiO}_2$  NFs are shown in Fig. 4. The Raman spectrum of  $\text{TiO}_2$  NFs shows clear signatures at about 397.5, 416.6, and 641  $\text{cm}^{-1}$ , as expected [26]. While the Raman spectrum of MWCNTs/ $\text{TiO}_2$  NFs shows both the features of  $\text{TiO}_2$  and the functionalized MWCNTs. For  $\text{COONH}_4$  functionalized MWCNTs, the Raman features observed at about 1363 and 1586  $\text{cm}^{-1}$  represented the disorder-induced D band and graphite carbon-related G band, respectively [27, 28]. The peak that is observed around 1620  $\text{cm}^{-1}$ , as a shoulder to the G band, can be caused by the oxidation of MWCNTs.

**Fig. 2** SEM surface morphology of the treated Ti surface in a mixed solution of  $\text{H}_2\text{O}_2$  (30 wt%) and NaOH (10 M) at 80 °C for 24 h, calcined at 400 °C for 1 h to obtain anatase NFs on the Ti substrate (**a, b**) and MWCNTs/ $\text{TiO}_2$  prepared by impregnation at 80 °C (**c, d**)

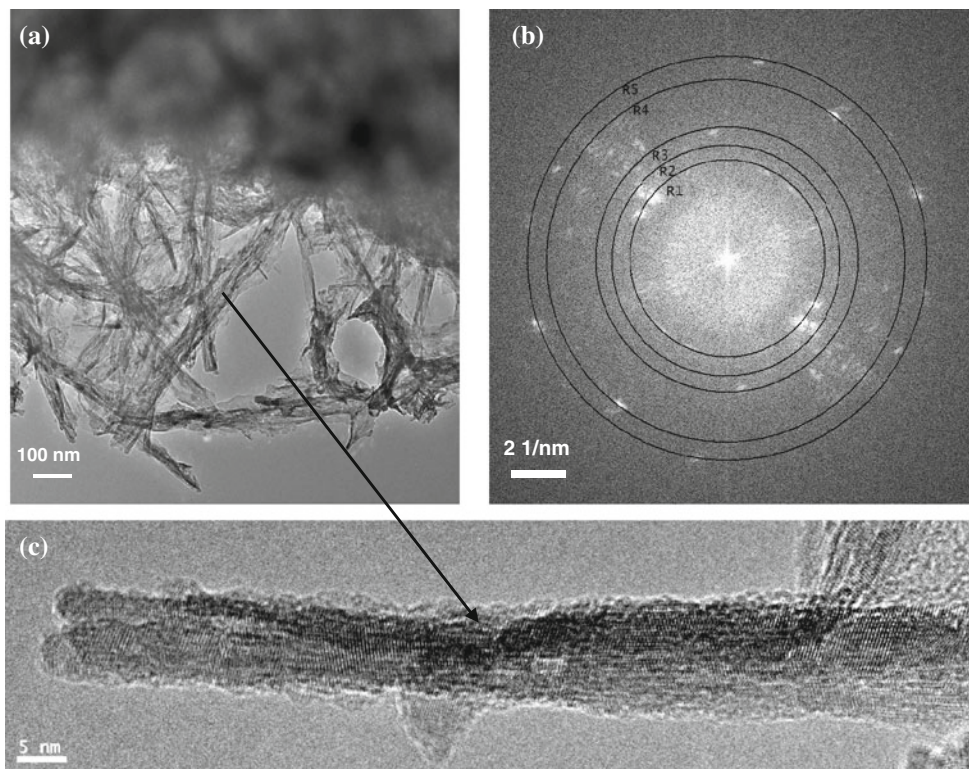
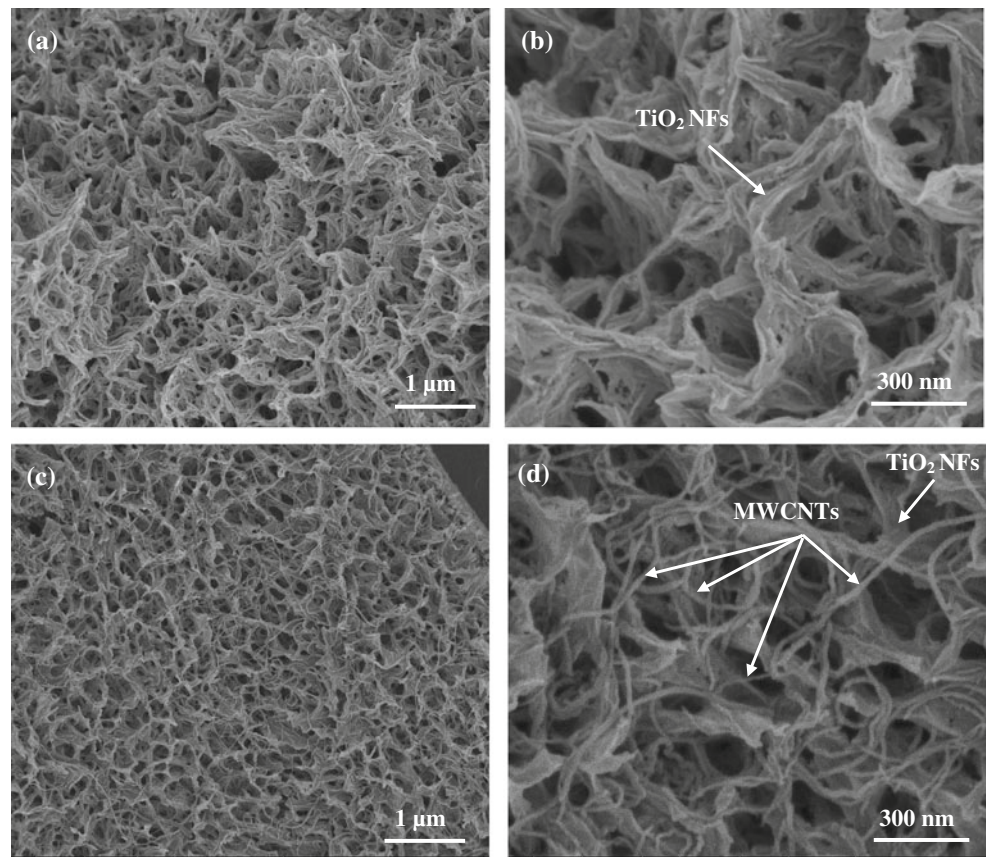


**Fig. 3** TEM image (**a**), electron diffraction pattern (**b**), and HRTEM image (**c**) of the powders scraped off from the treated Ti surface covered with  $\text{TiO}_2$  NFs

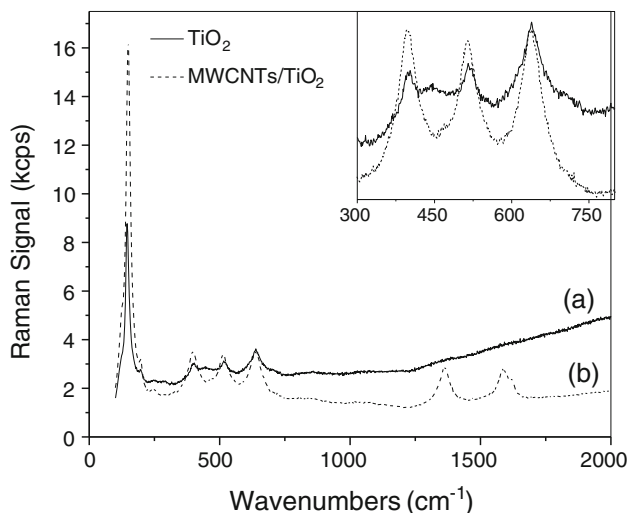


Fig. 4 Raman spectra of (a) TiO<sub>2</sub> NFs and (b) MWCNTs/TiO<sub>2</sub>

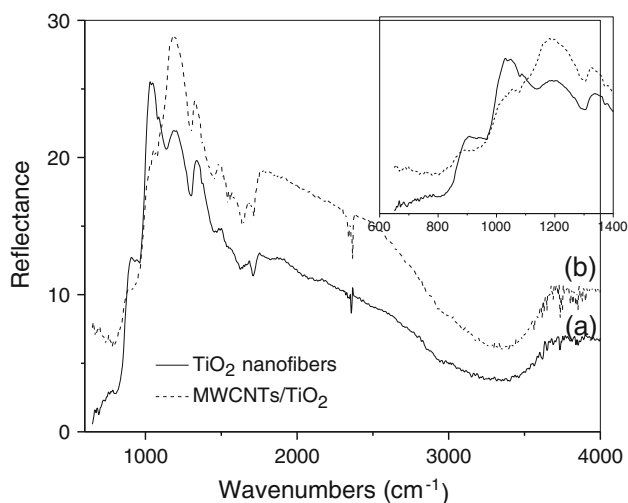


Fig. 5 FT-IR spectra of (a) TiO<sub>2</sub> NFs and (b) MWCNTs/TiO<sub>2</sub>

In addition, the intensity of the all Raman peaks is considerably enhanced in the case of MWCNTs/TiO<sub>2</sub> NFs. This may be explained by the existence of a small Surface Enhanced Raman Scattering effect which may appear as a result of the MWCNT incorporation.

FT-IR spectra of MWCNTs/TiO<sub>2</sub> NFs and pure TiO<sub>2</sub> NFs are presented in Fig. 5. The two spectra showed a similar shape. For MWCNTs/TiO<sub>2</sub> NFs, the band at 1550 cm<sup>-1</sup> is attributed to the C=C bond which indicates the presence of MWCNTs. The band at 1714 cm<sup>-1</sup> corresponds to C=O stretching of carboxylic groups [26], which confirms that the MWCNTs, integrated with the TiO<sub>2</sub> NFs, have been fully functionalized. This is in accordance with the results of Raman spectra described above. Both TiO<sub>2</sub> NFs and MWCNTs/TiO<sub>2</sub> NFs have the same broad peak near the 3400 cm<sup>-1</sup> corresponding to the stretching vibrations of O–H linkage on the TiO<sub>2</sub> surface

[29, 30]. As one can observe, the bands located at 1132 and 1296 cm<sup>-1</sup> which correspond to TiO<sub>2</sub> related vibrations, shift to lower binding energies when MWCNTs are incorporated. This may be due to the interaction between TiO<sub>2</sub> and CNTs.

XPS were acquired to confirm the MWCNTs integration with TiO<sub>2</sub> NFs. The XPS data from Ti, O, C, and N core levels of the MWCNTs/TiO<sub>2</sub> NF surface are shown in Figs. 6 and 7. Figure 6 shows the core-level BE values of bulk TiO<sub>2</sub> NFs; Ti 2p<sub>3/2</sub> at 458.3 eV and the Ti 2p<sub>1/2</sub> at 464 eV with spin-orbital splitting of 5.7 eV). But both Ti 2p<sub>3/2</sub> and Ti 2p<sub>1/2</sub> energies, measured from the MWCNTs/TiO<sub>2</sub> surface are shifted to higher binding energies by 0.5 eV. This shift may be due to the formation of CO–Ti(OH)<sub>3</sub> species that is explained by the chemical reactions below. The hydroxide group (OH) is more electronegative than CO group, so it interacts with the Ti atom by, either capturing its electrons or causing its polarization, thus leading to the rise of the BE. Since most metals are less electronegative than OH group, the formation of a hydroxide should be registered in XPS by an increase in BE of the Ti peak. Moreover, the O/Ti atomic ratio is calculated to be about 2.4 (Table 1), which is higher than the corresponding ratio for pure TiO<sub>2</sub> (Table 2). This may stem from the oxygen related to the oxidized MWCNTs that was attached to the Ti ions of TiO<sub>2</sub>. Figure 7 shows the corresponding high-resolution XPS and curve fittings of C 1s, O 1s and N 1s spectra where Fig. 7a, b present the high-resolution XPS data from C 1s core levels of the TiO<sub>2</sub> NFs before and after impregnation with MWCNTs, respectively. The C 1s peaks from the TiO<sub>2</sub> NFs before impregnation (Fig. 7a) can be fitted to four peaks. The BE of the contaminant carbon on the surface is assigned at 284.8 eV (C–C/C=C bonds). The three peaks with binding energies

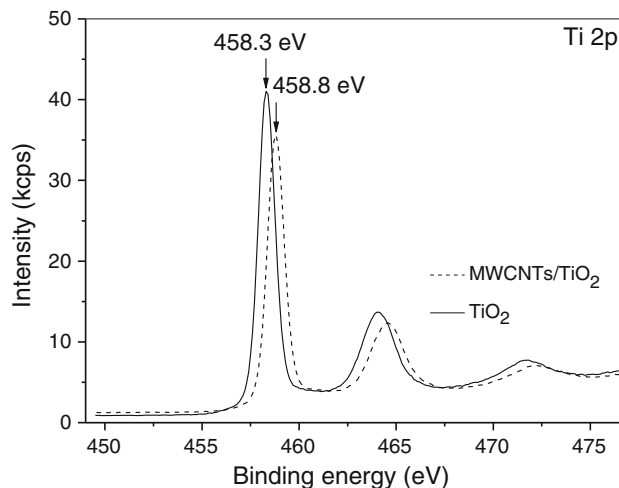
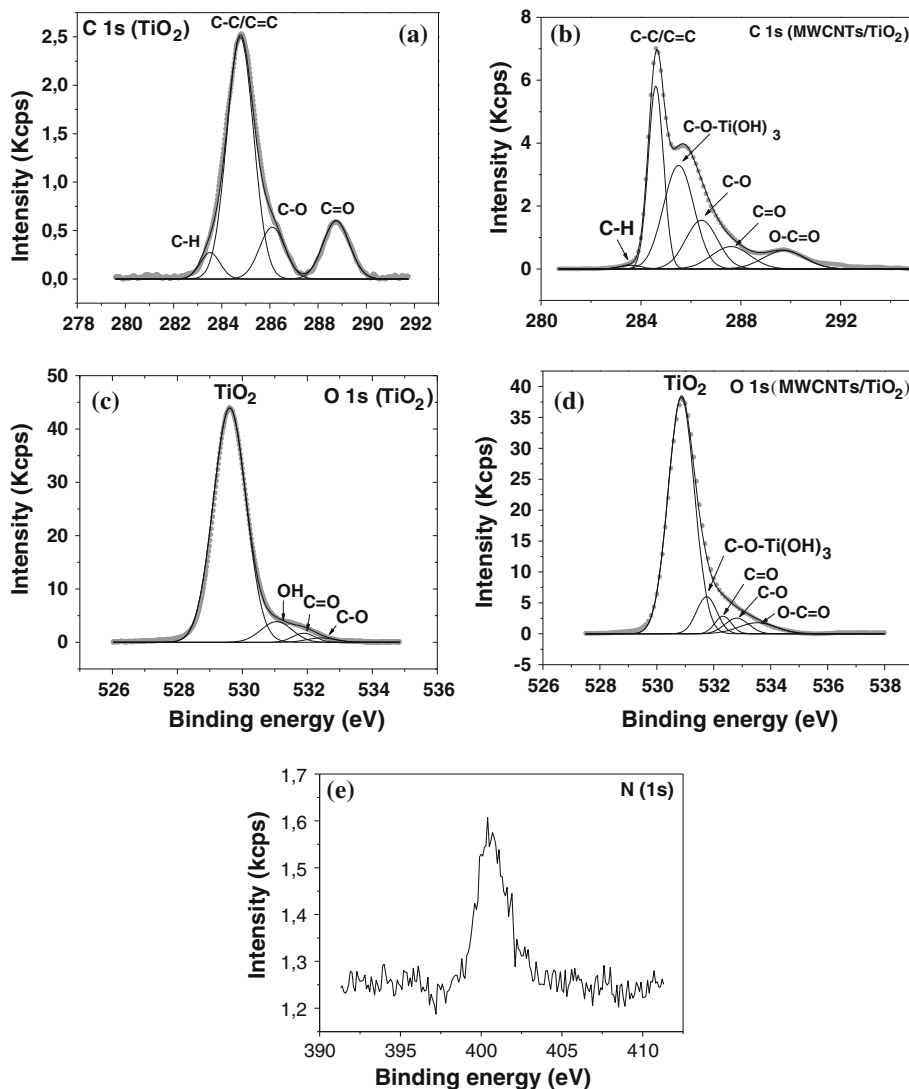


Fig. 6 XPS spectra of Ti2p core level of MWCNTs/TiO<sub>2</sub> in comparison with pure anatase TiO<sub>2</sub> NFs

**Fig. 7** XPS spectra of **a** C 1s and **c** O 1s core levels of TiO<sub>2</sub>, **b** C 1s, **d** O 1s, and **e** N 1s core levels of MWCNTs/TiO<sub>2</sub>



**Table 1** Atomic concentration deduced from the main XPS peaks of the MWCNTs/TiO<sub>2</sub> surface

Elements	O	C	Ti	N
Atomic concentration (%)	44.2	39.2	18.1	1.1

located at 284, 286.2, and 288.7 eV can be assigned to C–H, C–O, and C=O species, respectively [31–33]. After MWCNT integration, the C 1s band, considerably, increased in intensity and can be fitted to six peaks (Fig. 7b). The BE of MWCNTs and the contaminant carbon is assigned at 284.7 eV (C–C/C=C bonds). The four peaks with binding energies located at 283.5, 286.4, 288, and 289.8 eV can be assigned to C–H, C–O, C=O, and O–C=O species, respectively. The presence of the O–C=O species confirms that the MWCNTs, integrated into the composite, have been functionalized with carboxyl groups. The sixth peak appearing at about 285.6 eV may be attributed to the presence of CO/Ti(OH)<sub>3</sub> structure

**Table 2** Atomic concentration deduced from the main XPS peaks of the TiO<sub>2</sub> NF surface

Elements	O	C	Ti
Atomic concentration (%)	55.7	17.7	26.6

resulting from the interaction between the functionalized MWCNTs and TiO<sub>2</sub> NFs [34]. This peak confirms the linkage between the TiO<sub>2</sub> NFs and the MWCNTs.

Similarly, the O 1s spectrum of the TiO<sub>2</sub> NFs (Fig. 7c) can be fitted to four peaks located at 529.6, 531, 532, and 532.5 eV and attributed to TiO<sub>2</sub> NFs, OH [35], C=O, and C–O, respectively. After MWCNT integration, the O 1s peaks can be fitted to five peaks with four peaks located at 530.8, 532.3, 532.7, and 533.5 eV and attributed to TiO<sub>2</sub> NFs, C–O, C=O, and O–C=O, respectively [31]. The fifth peak located at 531.6 eV is assigned to the CO/Ti(OH)<sub>3</sub> structure [31]. These results provide further evidence that oxygen-based functional groups were linked to the TiO<sub>2</sub>

NFs network. As shown by the deconvoluted O 1s core level spectrum before and after MWCNTs impregnation (Fig. 7c, d), the fitted peak related to the TiO<sub>2</sub> NFs is shifted with 1.3 eV in the same direction of Ti 2p shift (mentioned above). The shift may be due to contribution from two effects: (1) the chemical shift related to OH attachment to Ti as explained above, (2) E<sub>F</sub> (Fermi level) shift which causes apparent rigid BE shift in the same direction irrespective of the atomic species involved, since the BE, by definition, is given as the energy difference from the E<sub>F</sub> [36, 37]. The high-resolution peak of N 1s (400.5 eV) can be attributed to the presence of pyrrolic/pyridine nitrogen [33] (Fig. 7d) resulting from MWCNT functionalization.

The possible interaction between the functionalized MWCNTs and TiO<sub>2</sub> NFs could be interpreted by means of chemical interaction between the modified MWCNTs and TiO<sub>2</sub> NFs. In our experiment we used ammonium salt of carboxylated carbon nanotubes (MWCNT–COONH<sub>4</sub>) to create chemical compatibility with the TiO<sub>2</sub> NFs surface. Such surface functional groups (O=C–O or COO<sup>–</sup>) provide active sites for directed reaction between anatase nanocrystals and MWCNTs [36]. For example, the –OH groups on the Titanium possibly react with the –OH and –COOH groups on the MWCNTs surface through esterification to form C–O–Ti or O=C–O–Ti bonds [38]. In this study, the chemical reactions between TiO<sub>2</sub> and MWCNTs–COONH<sub>4</sub> can be expressed as follows.

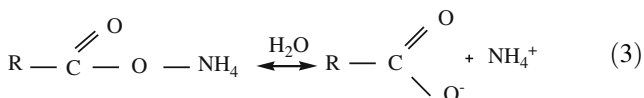
Initially, transition metal are, usually, highly reactive toward hydrolysis reaction which must take place first and form Ti hydroxide; Ti (OH)<sub>4</sub> [32]. The layer in contact with air submits hydrolysis reaction (1).



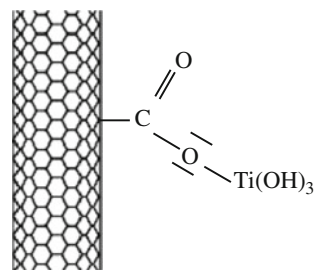
In water the resultant molecule decomposed to [Ti(OH)<sub>3</sub>]<sup>+</sup> with delocalized charge and a very small amount of Ti<sup>+</sup>(OH)<sub>3</sub> with localized charge on Ti atoms.



The used electrolyte R–COONH<sub>4</sub> (MWCNTs–COONH<sub>4</sub>) dissociates strongly in water even more than R–COOH (MWCNTs–COOH) by reaction 3:



MWCNTs — C(=O)O<sup>–</sup> reacts with the Ti<sup>+</sup>(OH)<sub>3</sub> in the solution as shown in Scheme 1.



**Scheme 1** Reaction of MWCNTs with TiO<sub>2</sub> NFs

There is an equilibrium reaction between [Ti(OH)<sub>3</sub>]<sup>+</sup> and Ti<sup>+</sup>(OH)<sub>3</sub> as shown in reaction (4).



K is the constant of instability ( $K = \frac{x}{n0-x}$ ) and in order to keep the equilibrium, the molecules Ti<sup>+</sup>(OH)<sub>3</sub> react with

MWCNTs — C(=O)O<sup>–</sup> leading to a transformation of [Ti(OH)<sub>3</sub>]<sup>+</sup> to Ti<sup>+</sup>(OH)<sub>3</sub>.

A HA layer was deposited on the TiO<sub>2</sub> NFs/Ti and MWCNTs/TiO<sub>2</sub>/Ti substrates through an electrodeposition process. The SEM images of the HA coating shown in Fig. 7 reveal a continuous and uniform HA coating with nanorice particle morphology for the two substrates; TiO<sub>2</sub> NFs (Fig. 8a, b) and HA/MWCNTs/TiO<sub>2</sub> structure (Fig. 8c, d). Compared to the HA layer deposited on the TiO<sub>2</sub> NFs only, the HA layer deposited on the TiO<sub>2</sub> impregnated with functionalized CNTs shows dense coating with nanorice particles, which may lead to higher adhesion strength and good corrosion resistance. To study the crystal structure of the nano-HA deposited on MWCNTs/TiO<sub>2</sub>/Ti substrate, we analyzed the XRD pattern of electrodeposited coatings before and after alkaline treatment. The XRD pattern (Fig. 9a) of the electrodeposited coating mostly consisted of calcium hydrogen phosphate (CaHPO<sub>4</sub>·2H<sub>2</sub>O, CHP) which transformed to HA in alkaline solution. The intense diffraction peaks shown in Fig. 9b at 25.84° and 32° belong to (002) and (211) crystal planes of HA coating, and the peaks at 33.26°, 34.17°, 35.19° also came from HA. The diffraction peak located at 25.3° is attributed to the anatase TiO<sub>2</sub> NFs.

In order to improve the crystallization and the interdiffusion between TiO<sub>2</sub> NFs and HA nanorice and relax the electrodeposition stresses [39], the samples were annealed in air at 900 °C for 1 h. The XRD pattern of the annealed samples (Fig. 9c), obviously, shows better crystallization of HA coating with sharp diffraction peaks, and anatase transformation to rutile with disappearance of the Ti peaks. This indicates that not only all the anatase transformed into

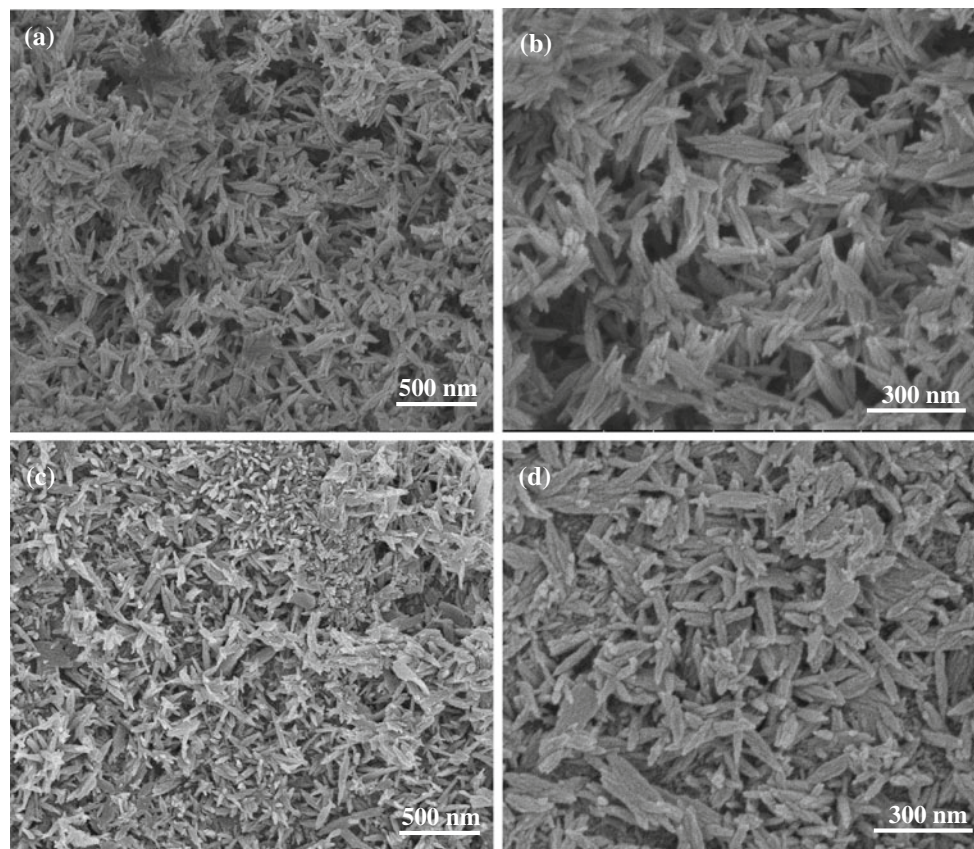


**Fig. 8** SEM images of the crystalline HA coated on **a, b** TiO<sub>2</sub> NFs and **c, d** MWCNTs/TiO<sub>2</sub> NFs. The HA appears as *nanorice grain-shaped*. They are fabricated by electrodeposition in an electrolyte

containing CaCl<sub>2</sub> and (NH<sub>4</sub>)<sub>2</sub>HPO<sub>4</sub> at constant potential of 3 V, then treated in an alkaline solution

rutile, but part of the Ti substrate, also, has oxidized to the rutile phase.

FT-IR spectrometry of the HA coating, after annealing, is shown in Fig. 10. Phosphate (PO<sub>4</sub><sup>3-</sup>)  $\nu_3$  vibration is found in the band region of 1065–1160 cm<sup>-1</sup> while phosphate  $\nu_1$  band is present at 973 cm<sup>-1</sup> [40]. The peaks in the region of 1377 and 1458 cm<sup>-1</sup> are due to  $\nu_3$  vibration mode of carbonate CO<sub>3</sub><sup>2-</sup> ion, indicating that part of calcium in HA transformed to CaCO<sub>3</sub> upon annealing. OH<sup>-</sup> composing HA related band is observed at about 1631 cm<sup>-1</sup>. There are faint absorptions at about 870 and 1226 cm<sup>-1</sup>, which belong to HPO<sub>4</sub><sup>2-</sup> bands [40]. Significant bands are also discerned between 2700 and 3050 cm<sup>-1</sup> that are due to adsorbed water. The characteristics of the spectrum are similar to those of mineral phase of bones [41].

Raman spectrum (Fig. 11a) from as-deposited HA/TiO<sub>2</sub>/Ti film exhibits bands at 142, 435, 593, 966, and 1075 cm<sup>-1</sup>. The first band corresponds to anatase NFs film that may originate from the under layer TiO<sub>2</sub>. The strongest band at 966 cm<sup>-1</sup> corresponds to the symmetric stretching mode  $\nu_1$  P–O of the tetrahedron PO<sub>4</sub><sup>3-</sup> [42]. The other bands observed in the frequency regions of 400–490,

570–625, and 1020–1075 cm<sup>-1</sup> are assigned to the  $\nu_2$ ,  $\nu_4$ , and  $\nu_3$  type of internal PO<sub>4</sub><sup>3-</sup> mode [42], respectively. Raman spectra of HA/TiO<sub>2</sub>/Ti and HA/MWCNTs/TiO<sub>2</sub>/Ti annealed at 900 °C (Fig. 11b, c) show all these bands along with TiO<sub>2</sub> rutile bands (442 and 606 cm<sup>-1</sup>), in addition to the frequency band situated at 230 cm<sup>-1</sup> which corresponds to the TiO<sub>2</sub> rutile structure. From these spectra, one can observe that the rutile bands in the HA/TiO<sub>2</sub>/Ti heat treated at 900 °C are strongest than the rutile bands observed in the HA/MWCNTs/TiO<sub>2</sub>/Ti heat treated at the same temperature (Fig. 11c). On the other hand, the strongest peak which corresponds to the HA structure is very weak in the case of the HA/TiO<sub>2</sub>/Ti film in comparison with the observed one in the HA/MWCNTs/TiO<sub>2</sub>/Ti layer. This indicates, also, that the HA coating on the MWCNTs/TiO<sub>2</sub> film is more dense and abundant than the HA coating on the TiO<sub>2</sub> NFs alone.

In order to confirm the effect of the multiwalled CNTs on the adhesion strength of the HA layer, we used scratching method that consists in moving an indenter (with pyramidal shape) on the surface of the specimens under an initial constant force (20 N). The applied force produces a damage of the film whose extent depends on the adherence. Clearly,



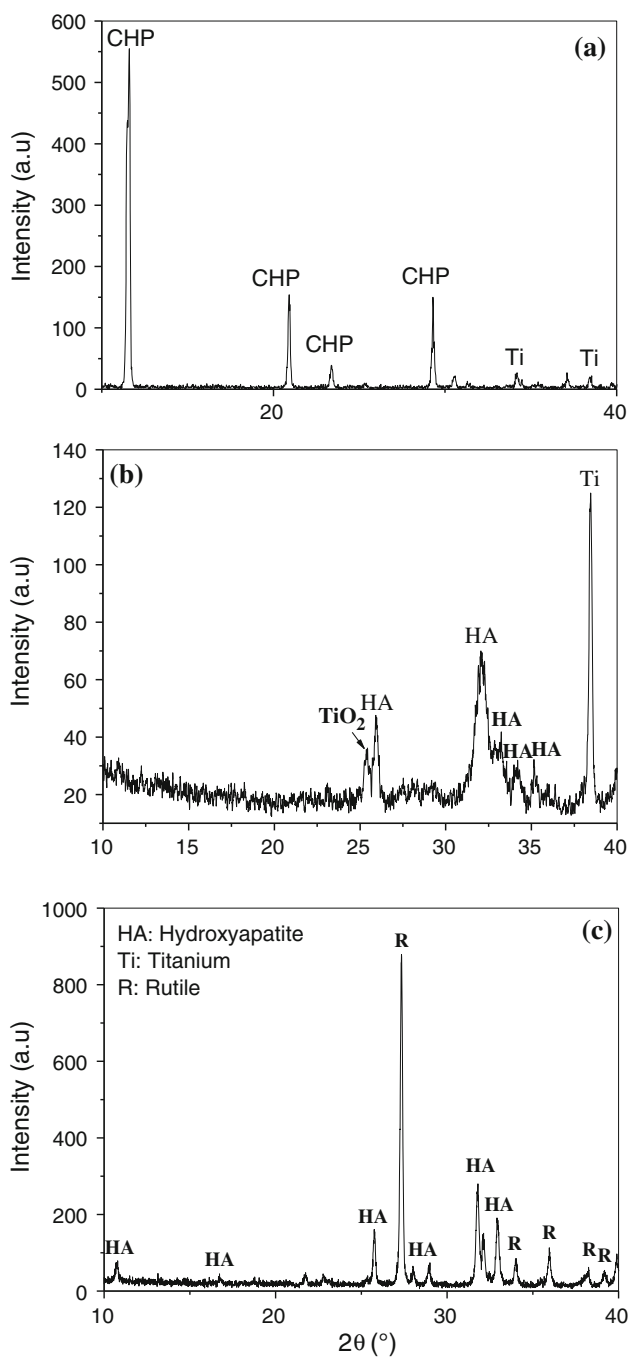


**Fig. 9** XRD patterns of the **a** as-prepared HA coating on TiO<sub>2</sub> NFs, which mostly consisted of CHP as a precursor of HA, **b** HA coating which originates from CHP transformation after treatment in NaOH and **c** the HA coated MWCNTs/TiO<sub>2</sub>/Ti sample and annealed at 900 °C for 1 h

it appears that MWCNT impregnation can improve the HA adhesion as can be seen in Fig. 12a, b. On the other hand, heat treatment at 900 °C under air can further enhance the adhesion strength as shown in Fig. 12c, d.

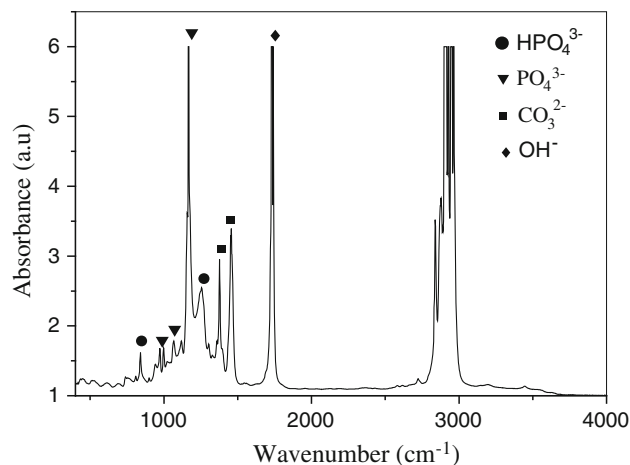


**Fig. 10** FT-IR spectrum of the HA deposited on MWCNTs/TiO<sub>2</sub>/Ti and annealed at 900 °C in air for 1 h

Metallic implants may be susceptible to corrosive attack by body fluids with subsequent release of metallic ions which might cause adverse effects to the surrounding tissues. Therefore, it is crucial to investigate the corrosion behavior of implant materials interacting with physiological environment. Figure 13 shows cyclic potentiodynamic polarization curves for TiO<sub>2</sub> NFs/Ti and HA/MWCNTs/TiO<sub>2</sub> coated Ti substrate. The corrosion parameters extracted from these curves (using special software: 352 soft Corr III) are shown in Table 3. It can be seen that both samples have very low anodic current density ( $I_{corr}$ ), compared to pure Ti foil (34.66  $\mu\text{A}/\text{cm}^2$ ) and nano-HA films (100  $\text{nA}/\text{cm}^2$ ) prepared by using electrophoretic method [42].  $I_{corr}$  values of the TiO<sub>2</sub> NFs/Ti and HA/MWCNTs/TiO<sub>2</sub> coatings are 0.044 and 0.025  $\text{nA}/\text{cm}^2$ , respectively. Compared to other works [40, 42], these anodic corrosion currents are almost negligible and present the lowest corrosion rate. One can observe, also, that HA-coated sample has the lowest current density and the highest corrosion resistance which is two times higher than that of TiO<sub>2</sub> NFs on Ti substrate. In addition, the anodic and cathodic potentiodynamic curves of the HA-coated sample are superposed with a potential of almost 0 mV (Fig. 13b) which is a further evidence of more stability. However, the anodic and cathodic curves corresponding to the TiO<sub>2</sub> NFs alone are not superposed, but the potential shifted towards noble metallic potential direction and reaches 260 mV (Fig. 13a). Moreover, no one of the tested sample exhibits appreciable hysteresis indicating the absence of passivity breakdown. Consequently, the coatings, effectively, act as a well barrier to the transport of electrons and ions between the substrate and the SBF solution.

**Fig. 11** Raman spectra of **a** non-annealed HA/TiO<sub>2</sub>/Ti, **b** annealed HA/TiO<sub>2</sub>/Ti, and **c** annealed HA/MWCNTs/TiO<sub>2</sub>/Ti at 900 °C

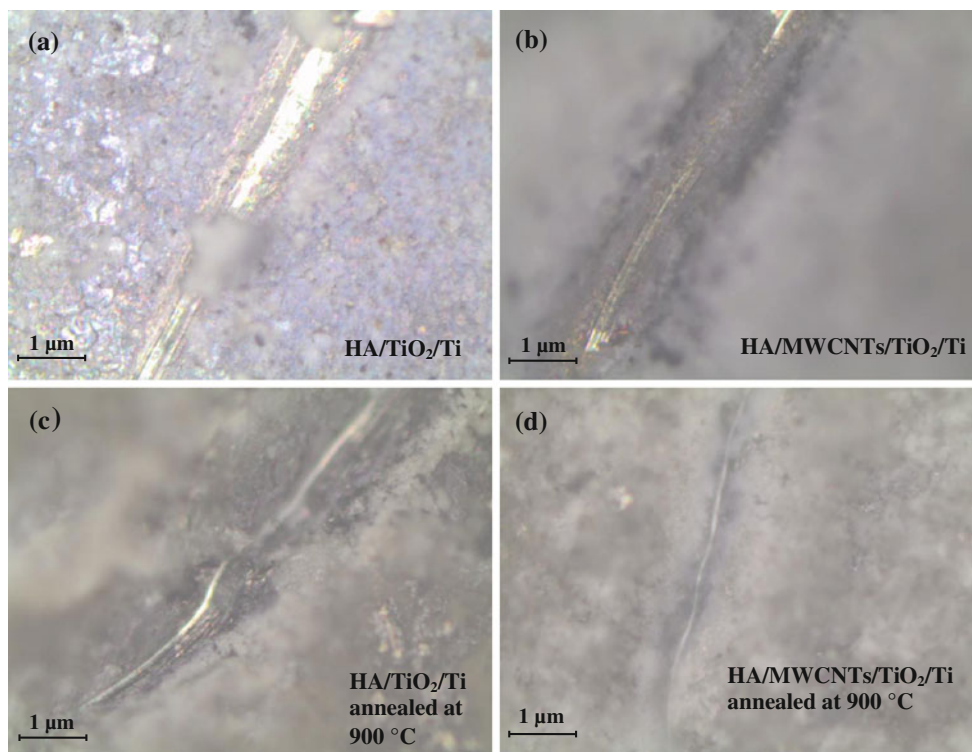
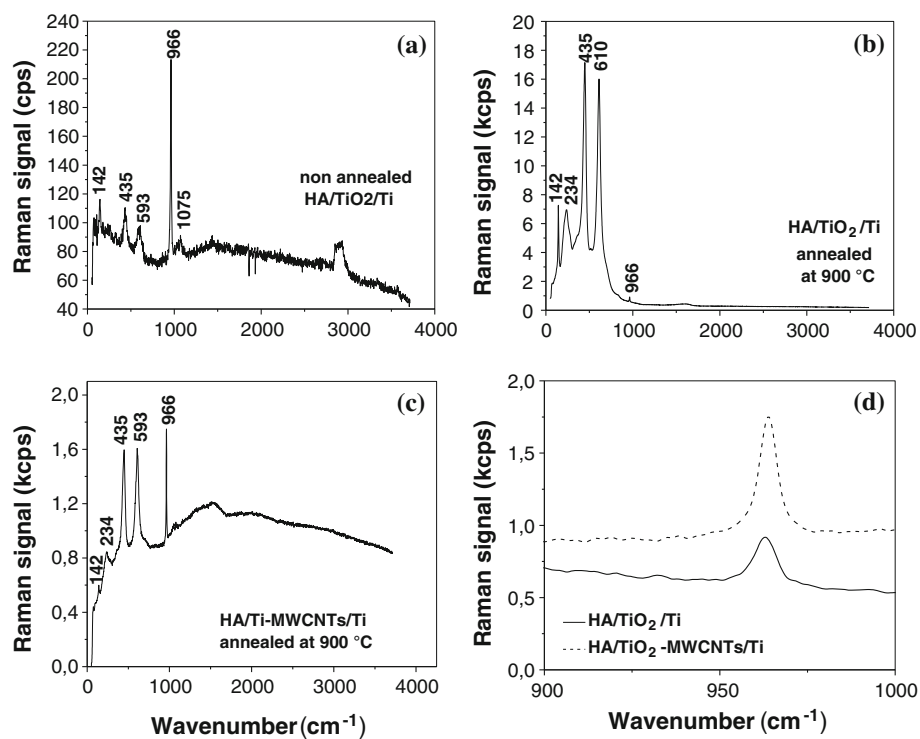


**Fig. 12** Optical micrographs of micro-scratching test of different sample surfaces: **a** HA/TiO<sub>2</sub>/Ti, **b** HA/MWCNTs/TiO<sub>2</sub>/Ti, **c** HA/TiO<sub>2</sub> annealed at 900 °C, and **d** HA/MWCNTs/TiO<sub>2</sub>/Ti annealed at 900 °C

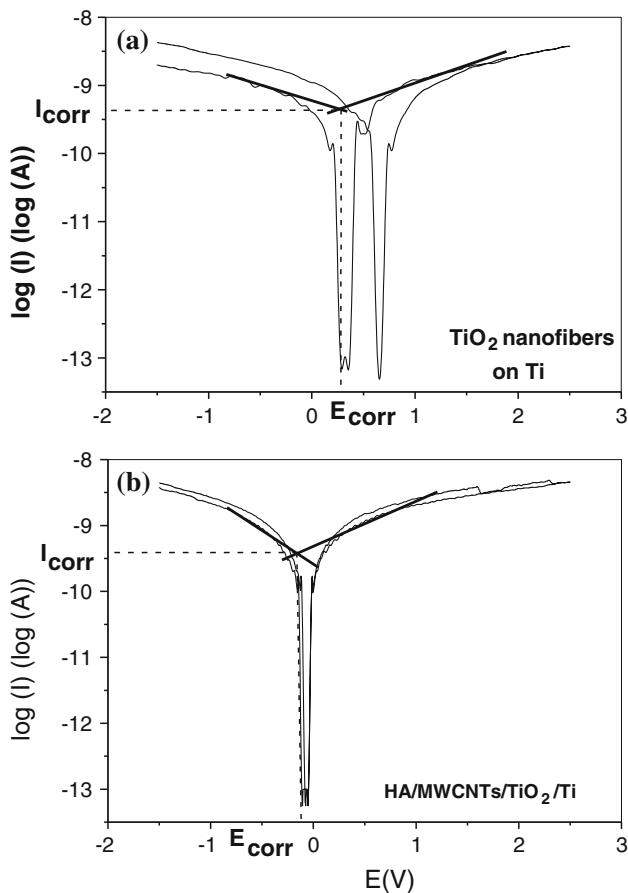


**Fig. 13** Potentiodynamic curves in simulated body fluid of TiO<sub>2</sub> NFs/Ti (a) and HA/MWCNTs/TiO<sub>2</sub>/Ti (b)

**Table 3** Results of electrochemical corrosion tests in SBF solution for both uncoated and HA/MWCNTs coated TiO<sub>2</sub> NFs

	Ti foil [42]	TiO <sub>2</sub> NFs	HA/MWCNTs/TiO <sub>2</sub> nanocomposite
$I_{corr}$	34.66 $\mu\text{A}/\text{cm}^2$	0.044 $\text{nA}/\text{cm}^2$	0.025 $\text{nA}/\text{cm}^2$
$E_{corr}$ (mV)	-246.7	268	0
$R_p$ (M $\Omega$ )		495	873.5

**Conclusions**

HA/MWCNTs/TiO<sub>2</sub> coatings were successfully fabricated on pure Ti substrate. Before coating, the Ti surface was chemically patterned with highly porous TiO<sub>2</sub> NFs network. Functionalized MWCNTs were successfully integrated between HA and TiO<sub>2</sub> NFs and showed a certain role in anchoring the HA coating. The microstructure analysis of HA/MWCNTs/TiO<sub>2</sub> surface showed homogeneous and dense nanorice particle morphology in comparison with the HA layer deposited on TiO<sub>2</sub> NFs only, which led to higher adhesion strength of the coating. The

adherence can be further improved by annealing and the obtained coatings show very good resistance corrosion in SBF solution.

**Acknowledgements** The authors acknowledge Professor C. Sahraoui from King Abdullah University of Science and Technology (KAUST) for his assistance in microanalysis and funding.

**References**

- Long M, Rack HJ (1998) *J Biomater* 19:1621
- Wang ZW, Wang YM, Liu Y, Xu JL, Guo LX, Zhou Y, Ouyang JH, Dai JM (2011) *J App Phys* 11:1405
- Macwan DP, Dave PN, Chaturvedi S (2011) *J Mater Sci* 46:3669. doi:10.1007/s10853-011-5378-y
- Afshar A, Yousefpour M, Yang XD, Li XD, Yang BC, Wu Y, Chen JY, Yang XD (2006) *J Mater Sci Eng B* 128:243
- Shaylin S, George JD (2012) *J Acta Biomater* 8:20
- Anselme K (2011) *J Osteoporos Int* 22:2037
- Xiao XF, Liu RF, Zheng YZ (2006) *J Surf Coat Tech* 200:4406
- Park JH, Lee DY, Oh KT, Lee YK, Kim KM, Kim N (2006) *J Mater Lett* 60:2573
- Guohua J, Xiaoyan Z, Yin W, Tianwen L, Xinke S (2011) *J Powder Technol* 207:465
- Lam CW, James JT, McCluskey R, Arepalli S, Hunter RL (2006) *J Crit Rev Toxicol* 36:189
- Jiang G, Wang L, Chen C, Dong X, Chen T, Yu H (2005) *J Mater Lett* 59:2085
- Teresa Cristina OM, Tiago GS, Cristina PS, Evaldo JC, Fernanda RM, Anderson OL (2012) *Langmuir* 28:4413
- Hsu CH, Liao HY, Kuo PL (2010) *J Phys Chem C* 14:7933
- Kauffman DR, Tang Y, Kichambare PD, Jackovitz JF, Star A (2010) *J Energ Fuel* 24:1877
- Suwilai C, Siwaporn M, Smith JS (2011) *J Microsc Soc Thail* 1:36
- Bai Y, Park I, Bae T, Kim K, Watari F, Uo M, Lee M (2011) *J Wuhan Univ Technol Mater Sci Ed* 5:867
- Baowan D, Triampo W, Triampo D (2009) *New J Phys* 11:093011
- Liu B, Zeng HC (2008) *J Chem Mater* 20:2711
- Kaya C (2008) *J Ceram Int* 34:1843
- Ji Xiaoli, Weiwei L, Qi W, Jianfeng M, Haihong X, Qing B, Chuantong L, Jinsong L (2012) *Int J Mol Sci* 13:5242
- Bokai Z, Chi TK (2011) *J Mater Sci Mater Med* 22:2249
- Zhengjie L, Lei C, Zengchao Z, Yueyun L, Yunhui D, Yubing S (2013) *J Mol Liq* 179:46
- Vassiliki K, Theodoros T, Theodora K, Antonios K, Konstantinos B, Jeff Th, Dimitrios G (2013) *J Mater Sci Eng B* 178:457
- Zhu L, Ye X, Tang G, Zhao N, Gong Y, Zhao Y, Zhao J, Zhang X (2006) *J Biomed Mater Res* 78A(2006):515
- Advincula MC, Petersen D, Rahemtulla F, Advincula R, Lemons JE (2007) *J Biomed Mater Res Part B* 80:107
- Peining Z, Nair AS, Shengyuan Y, Ramakrishna S (2011) *J Mat Res Bull* 46:588
- Frank O, Mohr M, Maultzsch J, Thomas C (2011) *J ACS NANO* 5:2231
- Zhang J, Zou HL, Qing Q, Yang YL (2003) *J Phys Chem B* 107:3712
- Wang H, Wang HL, Jiang WF (2009) *J Chemosphere* 75:1105
- Chena L, Pang X, Yua G, Zhanga J (2010) *J Adv Mater Lett* 1:75
- Kaciulis S, Mattogno G, Pandolfi L, Cavalli M, Gnappi G, Montenero A (1999) *J App Surf Sci* 151:1

32. Yan XB, Tay BK, Yang Y (2006) *J Phys Chem B* 110:25844
33. Achour A, Vizireanu S, Dinescu G, Le Brizoual L, Djouadi MA, Boujtita M (2013) *J App Surf Sci* 273:49
34. Wagner CD, Naumkin AV, Kraut-Vass A, Allison JW, Powell CJ, Rumble JR (2003) NIST Standard Reference Database 20, Version 3.5
35. Wang LQ, Baer DR, Engelhard MH, Shultz AN (1995) *J Surf Sci* 237:344
36. Min CH, Cho S, Lee SH, Cho DY, Park WG, Chung JG, Lee E, Lee JC, Anass B, Lee JH, Hwang CS, Oh SJ (2010) *J Appl Phys Lett* 96:201907
37. Achour A, Ait Aissa K, Mbarek M, El Hadj K, Ouldhamadouche N, Barreau N, Le Brizoual L, Djouadi MA (2013) *J Thin Solid Films* 538:71
38. Jiaguo Y, Tingting M, Shengwei L (2011) *J Phys Chem Chem Phys* 13:3491
39. Kar A, Raja KS, Misra M (2006) *J Surf Coat Technol* 201:3723
40. Mohan L, Durgalakshmi D, Geetha M, Sankara Narayanan TSN, Asokamani R (2012) *J Ceram Int* 38:3435
41. Ban S, Maruno S (1993) *J Appl Phys* 32(10B):1577
42. Rath PurnaC, Besra Laxmidhar, Singh BimalP, Bhattacharjee Sarama (2012) *J Ceram Int* 38:3209